ERROR SELF-COMPENSATION PHASE RETRIEVAL FOR BINARY FRINGE PROJECTION PROFILOMETRY

Anonymous authors
Paper under double-blind review

ABSTRACT

Binary-defocusing fringe projection profilometry (FPP) encodes sinusoidal fringes as 1-bit patterns to achieve high projection speed, but the binarization process introduces systematic phase bias and degrades reconstruction accuracy. Existing correction methods either require additional projections or rely on empirical compensation. In this paper, we analyze the forward and reverse Floyd–Steinberg (FS) error-diffusion processes and reveal the symmetry between their induced phase biases. Based on this observation, we propose an error self-compensation (ESC) framework that introduces reverse-diffused fringes to resolve the rank deficiency caused by binarization-induced unknown error terms, enabling unbiased wrapped-phase recovery without additional projections or post-processing. The proposed framework is applicable to phase-shifting schemes with more than three steps, while a double-binarization strategy is further developed for the under-constrained three-step case. The numerical stability of the phase solutions is analyzed, and the stable solution is identified for practical implementation. Extensive experiments demonstrate that ESC reduces the point-cloud MAE and RMSE by up to 84.8% and 80.3%, respectively, while maintaining robustness under varying projector defocus and dynamic measurement conditions.

1 INTRODUCTION

As industrialization and informatization advance rapidly, image information plays an increasingly important role. Because the information carried by traditional 2D images is limited, 3D shape information has become essential in aerospace, medical diagnosis, intelligent manufacturing, and the automotive industry (Chen et al., 2024; Wang, 2020; Liu et al., 2023). How to guarantee accuracy, completeness, and speed when acquiring 3D shape data has become a central research focus. Over the past decades, various non-contact 3D shape measurement techniques have been developed based on light, ultrasound, microwave, and electromagnetic waves. Among them, optical methods based on light propagation, reflection, and interference are the most widely used because of their high accuracy and speed. Representative optical techniques include binocular stereo vision (Chen et al., 2017), time-of-flight sensing (Palojarvi et al., 1996), speckle projection (Zhu et al., 2010), and structured light methods (Geng, 2011).

Fringe projection profilometry (FPP) based on structured light has become one of the mainstream approaches because of its simple setup and high accuracy (Xu & Zhang, 2020; Johnson et al., 2024; Zhang et al., 2022). Although FPP can provide stable and accurate point clouds, it still faces several bottlenecks. It requires projecting multiple fringe images, and when the measured object is non-stationary, phase-shift errors are inevitably introduced between frames (Zuo et al., 2018; Lu et al., 2014). As illustrated in Fig. 1, a camera pixel c_1 initially observes object point P_1 corresponding to projector phase p_1. After object motion, the same pixel observes another point P_2 corresponding to phase p_2. Such correspondence variation results in inaccurate phase recovery and degraded 3D reconstruction.

To alleviate motion-induced errors, reducing the number of required fringe images has become an important research direction. Binary fringe projection, which replaces conventional grayscale sinusoidal patterns with binary patterns, enables high-speed projection and reduces acquisition complexity. However, the binarization process inevitably introduces nonlinear intensity distortion after optical defocusing, leading to additional phase errors. These errors are particularly challenging

Reviewers: please read the Reviewer Guidelines (iclr.cc/Conferences/2027/ReviewerGuidelines) and the AI Policy for Reviewers (iclr.cc/Conferences/2027/AIPolicyForReviewers). If you used AI to expand, edit, or polish your review, please provide the input text to the LLM. Better still, consider skipping the LLM and submitting your original text: we, and the authors, are much more interested in your unedited thoughts than in what an LLM has to say. AI-assisted or not, you are putting your name and reputation behind your review: LLM-generated falsehoods, hallucinations or misrepresentations are subject to disciplinary action, which may include desk-rejecting all papers you have authored.

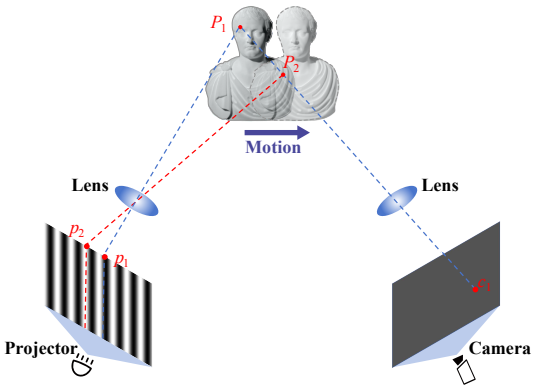

Figure 1: Schematic of the error caused by object motion.

because they are coupled with the phase-shifting process and cannot be completely eliminated by simply reducing the number of projected patterns. Therefore, understanding and compensating the intrinsic error mechanism of binary fringe projection is essential for achieving accurate high-speed FPP.

In this paper, we address the intrinsic directional bias in binary fringe generation by analyzing the forward and reverse Floyd–Steinberg (FS) error-diffusion processes. Instead of empirically correcting the recovered phase, the symmetry between their induced phase biases is exploited to develop a phase-shifting error self-compensation (ESC) framework. The main contributions are:

- The ESC method is constructed for phase-shifting schemes with more than three steps by introducing reverse-diffused fringes to eliminate the rank deficiency caused by additional unknown error terms introduced during binarization, thereby reducing systematic bias in wrapped-phase recovery.
- The ESC framework is further extended to the under-constrained three-step phase-shifting case through a double-binarization strategy, where the binarization error is compensated by sequential forward and reverse binarization processes.
- The numerical stability of ESC in multi-step phase shifting is analyzed, and the more stable solution is identified, providing a theoretical basis for practical implementation.
- The proposed method requires no additional projection or post-processing and introduces no additional measurement time or computational overhead. Extensive experiments demonstrate that it reduces the point-cloud MAE and RMSE by up to 84.8% and 80.3%, respectively.

2 Related Work

Direct motion-error compensation For phase-shift errors caused by object motion, directly compensating the error during reconstruction is a common and effective approach. Wang et al. (2018a) proposed a phase-compensation method based on the Hilbert transform, fusing the original phase-shift images with their transformed versions to reduce the influence of rigid and non-rigid motion. Feng et al. (2018) introduced an iterative motion-compensation method that requires no extra projections, correcting adjacent pixels through statistical analysis of the fringes, although its applicability to non-translational motion and complex deformation is limited. Liu et al. (2019) estimated the phase-shift error by averaging multiple sequences, which suits objects with large depth variation but assumes uniform translation. Wang et al. (2019) separated motion error by combining binary defocus with extra temporal sampling, which relaxes synchronization but involves multiple iterations. Overall, these methods rely on post-processing, and although they improve accuracy, they incur extra computation or acquisition overhead that limits dynamic-measurement efficiency.

Grating-image sharing Another direction aims to shorten the acquisition time by reducing the number of projected patterns per measurement. Zhong et al. (2013) shared phase-shifted fringes

across adjacent frames to increase the reconstruction frame rate. Wu et al. (2020) introduced a temporal-overlapping Gray-code strategy that reuses Gray-code patterns in phase-shifting sequences, reducing the required projections from seven to four while preserving dense reconstruction. A subsequent study further extended this idea by jointly reusing patterns and reducing the projection number to three (Wu et al., 2022). These methods improve measurement speed, but they do not fundamentally suppress the phase error induced by motion.

Scanning-speed improvement Increasing projection and acquisition rates shortens the acquisition interval, thereby reducing motion-induced errors. Binary-defocus projection exploits fast binary projection to generate quasi-sinusoidal fringes through optical defocusing while avoiding projector gamma nonlinearity (Li et al., 2024). However, residual higher-order harmonics distort the recovered phase, creating a trade-off between harmonic suppression and fringe contrast. Temporal coding (Ayubi et al., 2011; Zhu et al., 2016; Zhou et al., 2023) and phase-error compensation (Zhang, 2011; Wang et al., 2018b; Liu et al., 2015; Li et al., 2021; Yu & Da, 2021; Yang et al., 2025) alleviate this problem but may require additional projections, calibration, or computation. Alternatively, pulse-width modulation (Ayubi et al., 2010; Zuo et al., 2012; Wang & Zhang, 2010; Wang et al., 2017) and dithering (Wang & Zhang, 2012; Purgathofer et al., 1994; Bayer, 1976; Zhou et al., 2020a) improve the binary patterns themselves. Among dithering methods, error diffusion (Zhou et al., 2020a) has demonstrated superior performance in fringe generation, and several kernel-optimization methods have been proposed, including genetic-algorithm search (Lohry & Zhang, 2013), kernel-matrix expansion (Shan et al., 2023), joint kernel-and-threshold optimization (Zhu et al., 2024), intensity-and-phase joint optimization (Zhou et al., 2020b), and half-truncated sinusoidal fringes (You et al., 2022a). These methods improve binary fringe quality from different perspectives, but most lack an explicit criterion for eliminating directional bias introduced by diffusion kernels.

3 PRELIMINARIES

A typical FPP system consists of a digital projector, a camera, and the measured object. Pre-designed fringe patterns are projected onto the object surface and modulated by its 3D shape, after which the camera captures the deformed fringe images. The projected fringe pattern can be written as

$$I_n^p(x,y) = A + B\cos\left(\phi(x,y) + \delta_n\right), \quad n = 0, 1, 2, \ldots, N-1, \tag{1}$$

where $I_n^p(x,y)$ is the n-th phase-shifted fringe, (x,y) is the pixel coordinate on the projector plane, A and B are the average intensity and the intensity modulation, $\delta_n = 2\pi n/N$ is the phase shift, N is the total number of phase-shifting steps, and $\phi(x,y)$ is the wrapped phase to be solved. After phase unwrapping, camera–projector correspondences are established from the absolute phase, enabling 3D reconstruction through calibrated triangulation (Zhang, 2000).

The FS error-diffusion algorithm (Floyd, 1976) converts an 8-bit grayscale pattern into a binary pattern with only two gray levels. Each pixel is quantized by a preset threshold, and the residual quantization error is distributed to neighboring unprocessed pixels according to a diffusion kernel. This process is formulated as

$$\begin{aligned} I_n^{p\prime}(x,y) &= I_n^p(x,y) + \sum_{m,n\in\Omega} K(m,n)\, e(x-m, y-n), \\ e(x,y) &= I_n^{p\prime}(x,y) - I_n^b(x,y) = I_n^{p\prime}(x,y) - T\left[I_n^{p\prime}(x,y)\right], \end{aligned} \tag{2}$$

where, $e(x,y)$ is the quantization error, $T[\cdot]$ denotes the thresholding operation (typically with a threshold of 128), $I_n^{p\prime}(x,y)$ is the sum of the original pixel intensity and the accumulated error, $I_n^b(x,y)$ represents the resulting binary pattern after thresholding, K is the error-diffusion kernel, and Ω denotes its nonzero support. The forward and reverse FS kernels are centrally symmetric about the current pixel:

$$K_{\mathrm{FS}} = \frac{1}{16}\begin{bmatrix} - & \times & 7 \\ 3 & 5 & 1 \end{bmatrix}, \qquad K_{\mathrm{RFS}} = \frac{1}{16}\begin{bmatrix} 1 & 5 & 3 \\ 7 & \times & - \end{bmatrix}, \tag{3}$$

where, $\times$ marks the current pixel and $-$ denotes an already processed pixel. Forward FS scans from left to right and top to bottom, whereas reverse FS reverses both directions, scanning from right to left and bottom to top. This algorithm processes pixels in raster order, so the quantization error is systematically propagated toward the unprocessed neighbors.

Table 1: Mean projector-coordinate errors of forward FS and reverse FS (RFS) error diffusion at different fringe periods (unit: pixel).

Period	16	24	36	48	60	72	84	96	108	120
FS	0.159	0.190	0.191	0.194	0.196	0.194	0.192	0.194	0.196	0.195
RFS	−0.159	−0.193	−0.194	−0.198	−0.199	−0.198	−0.196	−0.197	−0.197	−0.197

4 Proposed Method

The analysis in Chen et al. (2026) indicates that binary fringes generated by forward and reverse FS error diffusion exhibit opposite intensity-error trends, resulting in phase errors of opposite signs. To examine this relationship quantitatively, simulations are conducted using the standard four-step phase-shifting algorithm with fringe periods ranging from 16 to 120 pixels. Projector defocus is modeled by a Gaussian filter with a 13×13-pixel kernel and a standard deviation of 3 pixels. As summarized in Table 1, forward and reverse FS error diffusion produce mean projector-coordinate errors of opposite signs and nearly equal magnitudes. Based on the above analysis, the fringe generated by the FS method after defocused projection and camera acquisition can be modeled as

$$I_n(x,y) = A + B\cos\left(\phi(x,y) + \delta + \delta_n\right), \quad n = 0,1,2,\ldots,N-1, \tag{4}$$

where, δ denotes the phase error introduced by binarization. Correspondingly, for the reverse FS method, the captured phase-shifted fringe is expressed as

$$I'_n(x,y) = A + B\cos\left(\phi(x,y) - \delta + \delta_n\right), \quad n = 0,1,2,\ldots,N-1. \tag{5}$$

As shown in Eq. (4), in the conventional FS dithering algorithm, the captured intensity $I_n(x,y)$ and the prescribed phase shift δ_n are known, whereas A, B, $\phi(x,y)$, and δ are unknown. By expanding the fringe model, the unknown parameters can be reformulated into five composite unknowns. Although five independent measurements are theoretically sufficient to recover these composite unknowns, the conventional phase-shifting scheme leads to a rank-deficient system, preventing unique recovery. Therefore, the five-step phase-shifting case is first analyzed to reveal the proposed error self-compensation principle, which is subsequently generalized to arbitrary phase-shifting patterns with $N > 3$. The three-step case is further discussed separately using a dedicated formulation.

4.1 Phase-shifting error self-compensation

For five-step phase shifting with $\delta_n = 2\pi n/5$, expanding the cosine term yields

$$\begin{aligned}
I_1 &= A + B\cos\delta\cos\phi - B\sin\delta\sin\phi,\\
I_2 &= A + \cos\tfrac{2\pi}{5}B\cos\delta\cos\phi - \sin\tfrac{2\pi}{5}B\cos\delta\sin\phi - \cos\tfrac{2\pi}{5}B\sin\delta\sin\phi - \sin\tfrac{2\pi}{5}B\sin\delta\cos\phi,\\
I_3 &= A + \cos\tfrac{4\pi}{5}B\cos\delta\cos\phi - \sin\tfrac{4\pi}{5}B\cos\delta\sin\phi - \cos\tfrac{4\pi}{5}B\sin\delta\sin\phi - \sin\tfrac{4\pi}{5}B\sin\delta\cos\phi,\\
I_4 &= A + \cos\tfrac{6\pi}{5}B\cos\delta\cos\phi - \sin\tfrac{6\pi}{5}B\cos\delta\sin\phi - \cos\tfrac{6\pi}{5}B\sin\delta\sin\phi - \sin\tfrac{6\pi}{5}B\sin\delta\cos\phi,\\
I_5 &= A + \cos\tfrac{8\pi}{5}B\cos\delta\cos\phi - \sin\tfrac{8\pi}{5}B\cos\delta\sin\phi - \cos\tfrac{8\pi}{5}B\sin\delta\sin\phi - \sin\tfrac{8\pi}{5}B\sin\delta\cos\phi.
\end{aligned} \tag{6}$$

For notational simplicity, the spatial coordinates (x,y) are omitted in these equations. Defining the unknown vector

$$\mathbf{x} = \left[A \quad B\cos\delta\cos\phi \quad B\cos\delta\sin\phi \quad B\sin\delta\sin\phi \quad B\sin\delta\cos\phi\right]^{\mathsf{T}}, \tag{7}$$

Eq. (6) can be written as the linear system

$$\mathbf{A}_0\mathbf{x} = \mathbf{b}_0, \tag{8}$$

with

$$\mathbf{A}_0 = \begin{bmatrix}
1 & 1 & 0 & -1 & 0\\
1 & \cos\frac{2\pi}{5} & -\sin\frac{2\pi}{5} & -\cos\frac{2\pi}{5} & -\sin\frac{2\pi}{5}\\
1 & \cos\frac{4\pi}{5} & -\sin\frac{4\pi}{5} & -\cos\frac{4\pi}{5} & -\sin\frac{4\pi}{5}\\
1 & \cos\frac{6\pi}{5} & -\sin\frac{6\pi}{5} & -\cos\frac{6\pi}{5} & -\sin\frac{6\pi}{5}\\
1 & \cos\frac{8\pi}{5} & -\sin\frac{8\pi}{5} & -\cos\frac{8\pi}{5} & -\sin\frac{8\pi}{5}
\end{bmatrix}, \quad \mathbf{b}_0 = \begin{bmatrix} I_1\\ I_2\\ I_3\\ I_4\\ I_5 \end{bmatrix}. \tag{9}$$

Inspecting $\mathbf{A}_0$, its second and fourth columns are linearly dependent, as are its third and fifth columns, so $\mathbf{A}_0$ is rank-deficient and Eq. (8) is ill-posed. To eliminate this linear dependence, the fourth and fifth phase-shifted patterns are replaced with fringes binarized by the reverse FS method. Their captured intensities become

$$I'_4 = A + B\cos\left(\phi(x,y) - \delta + \frac{6\pi}{5}\right), \quad I'_5 = A + B\cos\left(\phi(x,y) - \delta + \frac{8\pi}{5}\right). \tag{10}$$

By expanding Eq. (10) and substituting it into Eq. (6), we obtain the resulting coefficient matrix and observation vector:

$$\mathbf{A}'_0 = \begin{bmatrix} 1 & 1 & 0 & -1 & 0 \\ 1 & \cos\frac{2\pi}{5} & -\sin\frac{2\pi}{5} & -\cos\frac{2\pi}{5} & -\sin\frac{2\pi}{5} \\ 1 & \cos\frac{4\pi}{5} & -\sin\frac{4\pi}{5} & -\cos\frac{4\pi}{5} & -\sin\frac{4\pi}{5} \\ 1 & \cos\frac{6\pi}{5} & -\sin\frac{6\pi}{5} & +\cos\frac{6\pi}{5} & +\sin\frac{6\pi}{5} \\ 1 & \cos\frac{8\pi}{5} & -\sin\frac{8\pi}{5} & +\cos\frac{8\pi}{5} & +\sin\frac{8\pi}{5} \end{bmatrix}, \quad \mathbf{b}'_0 = \begin{bmatrix} I_1 \\ I_2 \\ I_3 \\ I'_4 \\ I'_5 \end{bmatrix}. \tag{11}$$

The columns of $\mathbf{A}'_0$ are now linearly independent, so the system is well-posed and can be uniquely solved as

$$\mathbf{x} = (\mathbf{A}'_0)^{-1}\mathbf{b}'_0. \tag{12}$$

Notably, the second and third elements of $\mathbf{x}$, namely $B\cos\delta\cos\phi$ and $B\cos\delta\sin\phi$, share the common factor $\cos\delta$. Their ratio therefore removes the influence of $\cos\delta$, yielding a phase estimate independent of the phase error δ:

$$\phi = \arctan\left(\frac{B\cos\delta\sin\phi}{B\cos\delta\cos\phi}\right) = \arctan\left(\frac{a_{31}I_1 + a_{32}I_2 + a_{33}I_3 + a_{34}I'_4 + a_{35}I'_5}{a_{21}I_1 + a_{22}I_2 + a_{23}I_3 + a_{24}I'_4 + a_{25}I'_5}\right), \tag{13}$$

where, a_{ij} is the (i,j)-th element of $(\mathbf{A}'_0)^{-1}$. Similarly, the fourth and fifth elements ($B\sin\delta\sin\phi$ and $B\sin\delta\cos\phi$) share the factor $\sin\delta$, yielding a second phase estimate:

$$\phi = \arctan\left(\frac{B\sin\delta\sin\phi}{B\sin\delta\cos\phi}\right) = \arctan\left(\frac{a_{41}I_1 + a_{42}I_2 + a_{43}I_3 + a_{44}I'_4 + a_{45}I'_5}{a_{51}I_1 + a_{52}I_2 + a_{53}I_3 + a_{54}I'_4 + a_{55}I'_5}\right). \tag{14}$$

This derivation reveals that conventional phase-shifting algorithms fail to compensate for dithering-induced errors because the error perturbation introduces linear dependence among the composite

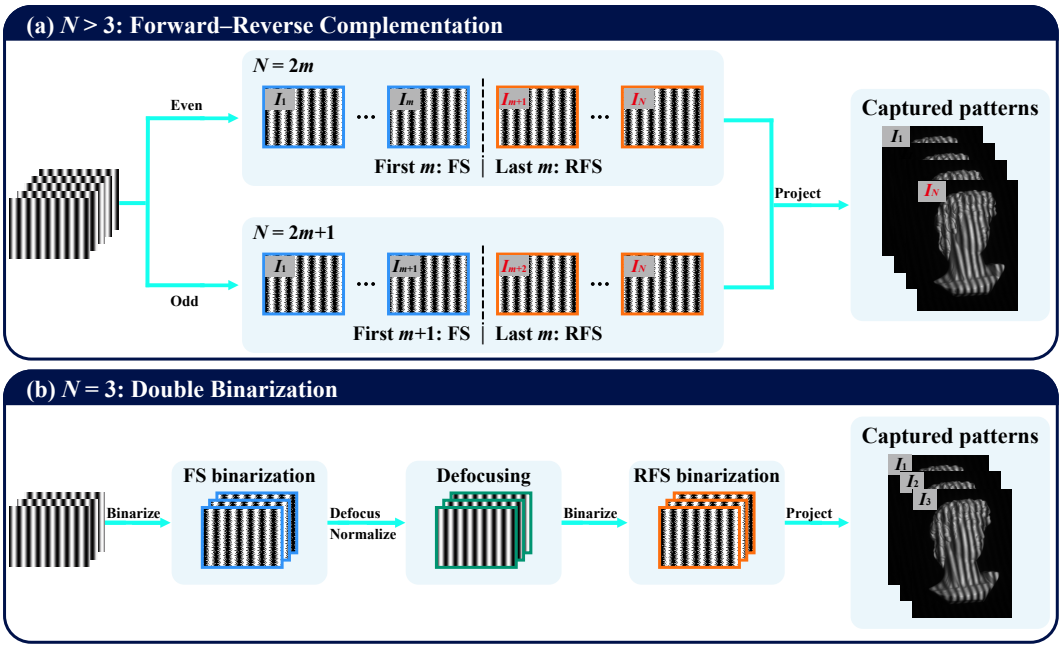

Figure 2: Flowchart of the error self-compensation method.

unknowns, making the original linear system unsolvable. By introducing reverse FS fringes and constructing a full-rank coefficient matrix $\mathbf{A}_0'$, the phase can be directly recovered from linear combinations of the captured fringes; the systematic phase bias induced by binarization is thereby canceled during phase retrieval without additional processing, as shown in Eqs. (13) and (14). Furthermore, the proposed self-compensation strategy can be extended from five-step phase shifting to arbitrary phase-shifting patterns with $N > 3$. As illustrated in Fig. 2(a), for $N = 2m$ ($m > 1$), the first m patterns are binarized using FS and the remaining m patterns using RFS; for $N = 2m + 1$, the first $m + 1$ patterns are binarized using FS and the remaining m patterns using RFS. EDF can be regarded as a special case of the proposed method when $N = 4$ (Chen et al., 2026).

Three-step case. For the under-constrained three-step phase-shifting case ($N = 3$), the captured fringes are insufficient to recover the five composite unknowns through the linear formulation described above. Therefore, a dedicated double-binarization strategy is adopted to compensate for the phase error before phase retrieval.

As illustrated in Fig. 2(b), each phase-shifting fringe is first binarized using the forward FS kernel. After defocusing and intensity normalization, the binary fringe is converted into a full-contrast quasi-sinusoidal fringe. According to Eq. (4), this intermediate fringe can be expressed as

$$\bar{I}_n = A + B\cos(\phi + \delta + \delta_n), \quad n = 0, 1, 2. \tag{15}$$

The intermediate fringe is subsequently binarized using the reverse FS kernel. Since the reverse FS process introduces a phase bias with opposite sign, the final captured fringe can be expressed as

$$I_n^d = A + B\cos((\phi + \delta) - \delta + \delta_n) = A + B\cos(\phi + \delta_n), \quad n = 0, 1, 2. \tag{16}$$

Therefore, the phase error introduced by the first binarization is canceled during the second binarization process, and the resulting three fringes become equivalent to ideal three-step phase-shifting patterns. The wrapped phase can then be recovered by the standard three-step phase-shifting formula:

$$\phi = -\arctan\frac{\sqrt{3}(I_1^d - I_2^d)}{2I_0^d - I_1^d - I_2^d}. \tag{17}$$

The algorithms in Fig. 2 share the same principle of achieving error self-compensation through either the binarization process or the generated binary fringes themselves. Since the compensation is performed before fringe projection, these methods introduce no additional measurement time or computational cost. This pre-compensation strategy is termed error self-compensation (ESC) algorithm in this paper.

4.2 Numerical stability of the two phase solutions

Although both solutions in Eqs. (13) and (14) can theoretically recover the correct phase, they exhibit different numerical stability in practice. Hereafter, the solutions in Eqs. (13) and (14) are denoted as ESC and ESC$'$, respectively. As presented in Fig. 3, under Gaussian-filtering-based defocus simulation for five-step phase shifting, ESC yields a smooth and stable phase distribution, whereas ESC$'$ suffers from noticeable noise fluctuations. The mean phase error of ESC is 0.0097 rad, which is lower than those of the FS method (0.0756 rad) and ESC$'$ (0.0544 rad).

The instability of ESC$'$ arises from division by a small denominator. In the ideal model,

$$\tan\phi = \frac{B\sin\delta\sin\phi}{B\sin\delta\cos\phi}. \tag{18}$$

However, in practical systems, the numerator and denominator are perturbed to $\sin\delta + \varepsilon_1$ and $\sin\delta + \varepsilon_2$ with $|\varepsilon_1|, |\varepsilon_2| \ll 1$. When δ approaches 0, $\sin\delta \approx \delta$, giving

$$\tan\phi' \approx \frac{(\delta + \varepsilon_1)}{(\delta + \varepsilon_2)}\tan\phi. \tag{19}$$

The relative error is therefore

$$\frac{\tan\phi' - \tan\phi}{\tan\phi} \approx \frac{\varepsilon_1 - \varepsilon_2}{\delta + \varepsilon_2}, \tag{20}$$

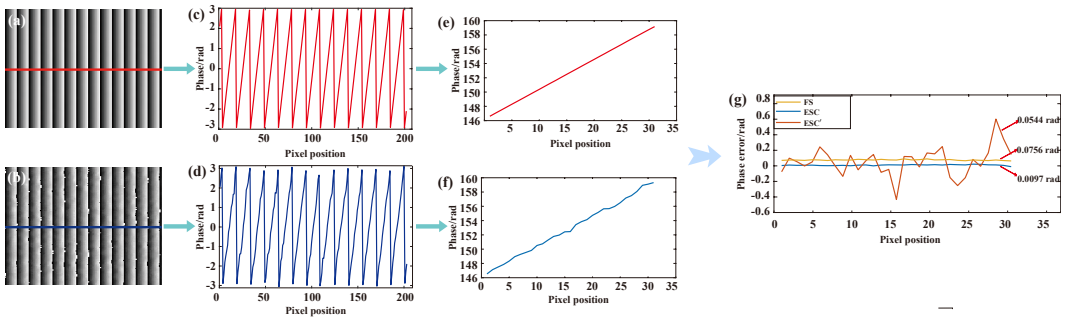

Figure 3: Simulation comparison of the two phase solutions: (a) Wrapped phase by ESC; (b) Wrapped phase by ESC′; (c) Cross-section of the red region in (a); (d) Cross-section of the blue region in (b); (e) Absolute phase by ESC; (f) Absolute phase by ESC′; (g) Phase-error curves of the compared methods.

which is amplified by the small denominator. In contrast, ESC divides perturbed cosine terms, i.e., $\cos\delta + \varepsilon_3$ and $\cos\delta + \varepsilon_4$. Since $\cos\delta \approx 1 - \delta^2/2$ when δ approaches 0, the denominator remains close to 1 and avoids small-denominator amplification:

$$\frac{\tan\phi'' - \tan\phi}{\tan\phi} \approx \frac{\varepsilon_3 - \varepsilon_4}{1 - \delta^2/2 + \varepsilon_4}. \tag{21}$$

Therefore, Eq. (13) is numerically more robust.

5 Experiments

To verify the feasibility and effectiveness of the proposed method, a hardware platform consisting of a DLP projector (LightCrafter 4500, 912×1140 pixels) and an industrial camera (MV-CS004-10UM, 720×540 pixels) is built. System calibration follows Zhang (2000). The wrapped phase is recovered using phase shifting, and complementary Gray-code patterns are employed for phase unwrapping. The ESC method is compared with conventional FS error diffusion (Floyd, 1976), Sierra-Lite (SL) error diffusion (Lv et al., 2014), the strip half-cutting method (SHM) (You et al., 2022a), and the direct compensation method (DCM) (You et al., 2022b). Fringes with a 15-pixel period are projected, and standard 8-bit sinusoidal fringes are used to generate the reference ground truth. Additional experimental results are provided in **Appendix** A.

5.1 Numerical-stability validation

The numerical stability of ESC and ESC′ is evaluated on a standard stepped block. Five-step phase shifting is adopted, and binary fringes generated by ESC and ESC′ are projected onto the block under moderate defocus. Figs. 4(b) and (c) present the recovered absolute phases. The cross-sectional profile obtained using ESC exhibits substantially fewer fluctuations than that obtained using ESC′, which agrees well with the simulation results and the theoretical analysis in Section 4.2. Therefore, ESC is adopted in all subsequent experiments.

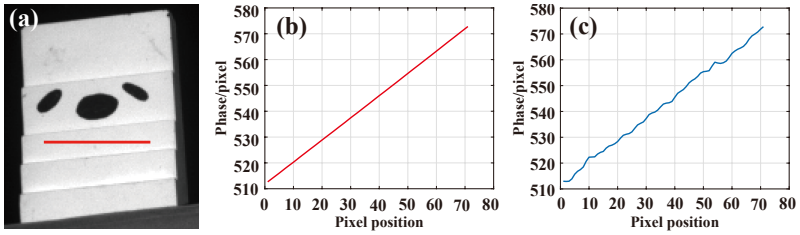

Figure 4: Phase results on the standard stepped block: (a) the measured block; (b) absolute phase by ESC; (c) absolute phase by ESC′.

The recovered absolute phase is converted into 3D point-cloud coordinates using the calibrated system parameters. The following experiments evaluate the reconstruction accuracy of ESC under different projector defocus levels and across objects with different surface geometries.

5.2 Point-cloud reconstruction under varying defocus

To evaluate the robustness of ESC to projector defocus, a white board is measured under slight, moderate, and strong defocus. Fig. 5 presents the captured Gray-code patterns and the corresponding point-cloud error distributions. The progressively blurred Gray-code edges indicate increasing defocus. The MAE and RMSE are calculated against the reference point cloud reconstructed using 8-bit sinusoidal fringes. As summarized in Table 2, ESC achieves the lowest MAE and RMSE under all three conditions. The best and second-best results are highlighted in red and blue, respectively. Under slight, moderate, and strong defocus, ESC reduces MAE by 67.1%, 82.2%, and 75.3%, respectively, relative to FS, with corresponding RMSE reductions of 62.8%, 78.2%, and 70.6%. Compared with the second-best method, DCM, ESC further reduces the MAE by 32.5%, 29.5%, and 20.5%, and the RMSE by 28.6%, 27.2%, and 18.6%, respectively. Moderate defocus effectively converts binary fringes into near-sinusoidal patterns while preserving sufficient modulation amplitude, allowing ESC to achieve its lowest reconstruction errors.

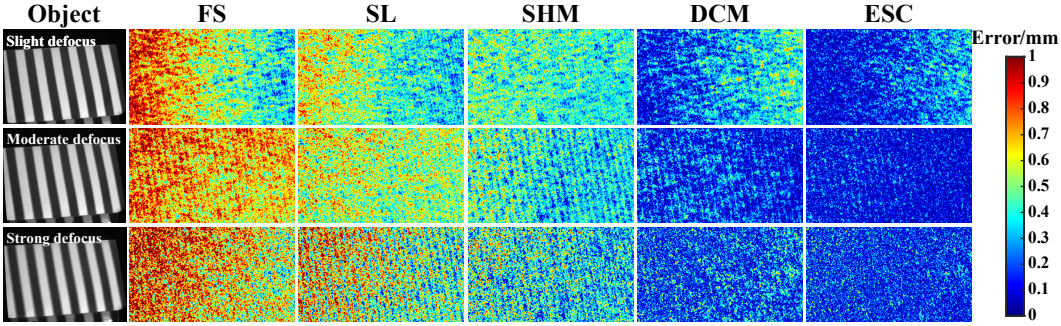

Figure 5: Point-cloud reconstruction errors of the white board under varying projector defocus. Rows from top to bottom correspond to slight, moderate, and strong defocus. Columns from left to right show the captured Gray-code patterns and the absolute point-cloud error distributions obtained by FS, SL, SHM, DCM, and ESC.

Table 2: MAE / RMSE of the white board under different projector defocus levels (unit: mm).

Defocus	FS	SL	SHM	DCM	ESC
Slight	0.575/0.611	0.468/0.493	0.423/0.438	**0.280/0.318**	**0.189/0.227**
Moderate	0.696/0.712	0.541/0.557	0.382/0.407	**0.176/0.213**	**0.124/0.155**
Strong	0.691/0.727	0.536/0.584	0.375/0.419	**0.215/0.263**	**0.171/0.214**

5.3 Point-cloud reconstruction of different objects

To evaluate the reconstruction accuracy of ESC across different surface geometries, a standard stepped block, a doll, and two sculptures (Mars and Venus) are measured. These objects include planar steps, curved surfaces, and fine geometric details. Fig. 6 presents the measured objects and the corresponding point-cloud error distributions, while Table 3 summarizes the MAE and RMSE.

ESC consistently achieves the lowest MAE and RMSE for all four objects. For the stepped block, ESC reduces the MAE and RMSE by 83.3% and 79.7% relative to FS, and by 41.4% and 37.2% relative to the second-best method, DCM. For the doll, the corresponding reductions are 83.9% and 78.6% relative to FS, and 24.3% and 19.4% relative to DCM. The improvement is also maintained on the sculptures: for Mars, ESC reduces the MAE and RMSE by 82.3% and 77.4% relative to FS, and by 20.2% and 16.7% relative to DCM; for Venus, the reductions are 84.8% and 80.3% relative to FS, and 26.6% and 22.3% relative to DCM. These results demonstrate that ESC improves reconstruction accuracy across both simple and complex surface geometries.

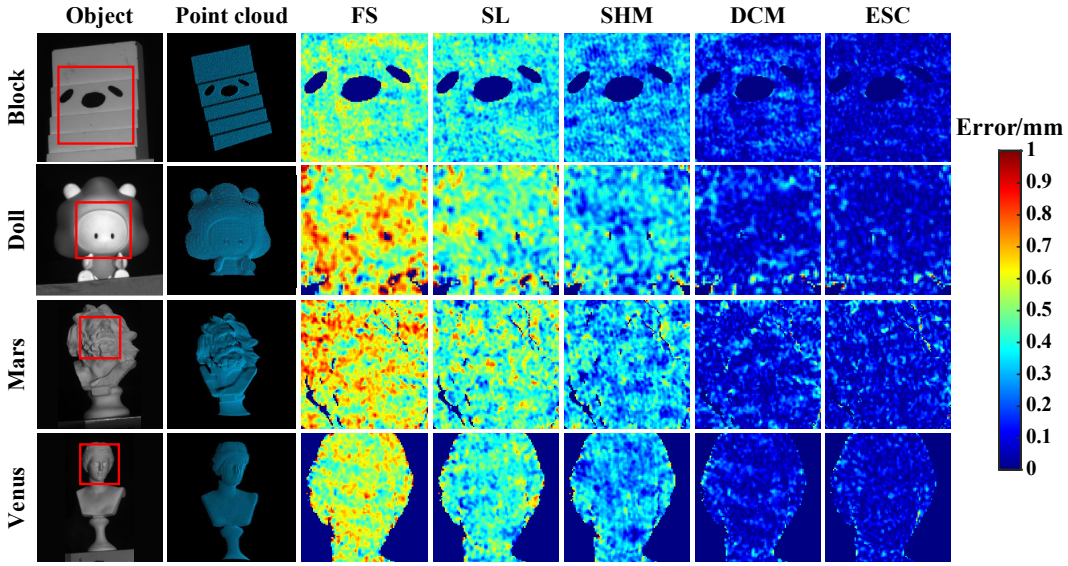

Figure 6: Point-cloud error distributions for different objects. From top to bottom: the standard stepped block, doll, Mars sculpture, and Venus sculpture. From left to right: the measured objects with evaluation regions outlined in red, the point clouds and the error distributions obtained using FS, SL, SHM, DCM, and ESC.

Table 3: MAE/RMSE of point-cloud reconstruction for different objects (unit: mm).

Object	FS	SL	SHM	DCM	ESC
Block	0.435/0.458	0.347/0.367	0.259/0.278	**0.124/0.148**	**0.073/0.093**
Doll	0.577/0.599	0.446/0.466	0.317/0.337	**0.123/0.159**	**0.093/0.128**
Mars	0.580/0.598	0.445/0.463	0.313/0.335	**0.129/0.162**	**0.103/0.135**
Venus	0.414/0.482	0.317/0.374	0.227/0.272	**0.086/0.122**	**0.063/0.095**

6 LIMITATIONS

This work has two main limitations. First, the proposed ESC framework is established based on the forward–reverse symmetry of phase biases in FS error diffusion. Although FS is one of the most widely used error-diffusion kernels, whether other diffusion kernels exhibit similar bias symmetry remains unclear. Therefore, extending the proposed compensation principle to more general binary encoding schemes or diffusion strategies requires further investigation of their corresponding bias characteristics. Second, although ESC effectively suppresses the binarization-induced phase bias, residual errors caused by non-ideal binarization effects and higher-order errors still leave room for further improvement in compensation accuracy.

7 CONCLUSION

In this work, we revealed the forward–reverse symmetry of the phase biases introduced by Floyd–Steinberg error diffusion and developed an error self-compensation (ESC) framework for accurate binary fringe projection profilometry. By incorporating reverse-diffused fringes or double binarization, ESC effectively eliminates the binarization-induced phase bias for both multi-step and three-step phase-shifting schemes without additional projections or post-processing. The numerical stability of ESC was further analyzed to determine the reliable solution for practical applications. Extensive experiments under various defocus conditions and measurement scenarios demonstrated that ESC significantly improves phase accuracy and three-dimensional reconstruction quality, providing an efficient solution for high-speed binary fringe projection measurement.

AI USE STATEMENT

In this work, we used generative AI tools to assist with translation, edit the research paper to improve readability, and format references. We have not used generative AI tools to help develop theoretical models or conceptual frameworks, formulate mathematical claims, provide critical ingredients for proving mathematical claims, assist in the writing of proofs, propose or refine hypotheses, design or provide feedback on research methodology or experiments, implement methods, support qualitative and thematic data analysis, or interpret results. Generative AI tools were not used to generate synthetic datasets, clean or reformat datasets, as these tasks are not applicable to this work. Additionally, we used generative AI tools for proposing a title and keywords. We have reviewed all AI-assisted work. We take responsibility for the final content of this work, including text, claims, and artifacts produced with the aid of generative AI.

ETHICS STATEMENT

This work does not involve human subjects, animal experiments, personal data, or other foreseeable ethical concerns.

REPRODUCIBILITY STATEMENT

The derivations of the proposed error self-compensation (ESC) framework are presented in Section 4. The experimental setup, parameter settings, and evaluation details are reported in Section 5 and the corresponding tables. Since ESC is an analytical method without learned components, all necessary details for reproduction are provided.

REFERENCES

Gaston A. Ayubi, Jaime A. Ayubi, J. Matias Di Martino, and Jose A. Ferrari. Pulse-width modulation in defocused three-dimensional fringe projection. *Optics Letters*, 35(21):3682–3684, 2010. ISSN 0146-9592.

Gaston A. Ayubi, J. Matias Di Martino, Julia R. Alonso, Ariel Fernandez, Cesar D. Perciante, and Jose A. Ferrari. Three-dimensional profiling with binary fringes using phase-shifting interferometry algorithms. *Applied Optics*, 50(2):147–154, Jan 10 2011. ISSN 1559-128X.

Bryce E. Bayer. An optimum method for two-level rendition of continuous-tone pictures. In *Proceedings of International Conference on Communications*, pp. 69–77, 1976.

Sisi Chen, Zhanguo Li, Yaochen Shi, and Yunguang Cai. Research on stamping die reconstruction method based on binocular stereo vision. In *Proceedings of the 6th International Conference on Energy and Environmental Protection*, pp. 985–988, 2017.

Yuchong Chen, Jian Yu, Pengcheng Yao, Shaoyan Gai, and Feipeng Da. Modeling and compensating phase error in high-speed 3d reconstruction. In *Computer Vision – ECCV 2026*. Springer, 2026.

Ze Chen, Mulun Zhu, Chuanzhi Sun, Yongmeng Liu, and Jiubin Tan. Fringe projection profilometry for three-dimensional measurement of aerospace blades. *Symmetry*, 16(3):350, 2024.

Shijie Feng, Chao Zuo, Tianyang Tao, Yan Hu, Minliang Zhang, Qian Chen, and Guohua Gu. Robust dynamic 3-d measurements with motion-compensated phase-shifting profilometry. *Optics and Lasers in Engineering*, 103:127–138, Apr 2018. ISSN 0143-8166.

Robert W Floyd. An adaptive algorithm for spatial gray-scale. In *Proceedings of the Society for Information Display*, pp. 75–77, 1976.

Jason Geng. Structured-light 3d surface imaging: a tutorial. *Advances in Optics and Photonics*, 3 (2):128–160, JUN 2011. ISSN 1943-8206.

Steven Johnson, Hal Gee, Faith Nwachi, and Simon Peter Mekhail. Fiber-based high-speed fringe projection profilometry. *Optics and Laser Technology*, 177:111173, 2024. ISSN 0030-3992.

Yueyang Li, Junfei Shen, Zhoujie Wu, and Qican Zhang. Passive binary defocusing for large depth 3d measurement based on deep learning. *Applied Optics*, 60(24):7243–7253, Aug 20 2021. ISSN 1559-128X.

Yueyang Li, Zhoujie Wu, and Qican Zhang. Phase error compensation technique based on phase-shifting fringe analysis: a review (invited). *Laser & Optoelectronics Progress*, 61(2):0211008, 2024. ISSN 1006-4125.

Xinran Liu, Tianyang Tao, Yingying Wan, and Jonathan Kofman. Real-time motion-induced-error compensation in 3d surface-shape measurement. *Optics Express*, 27(18):25265–25279, Sep 2 2019. ISSN 1094-4087.

Yuankun Liu, Qican Zhang, and Xianyu Su. 3d shape from phase errors by using binary fringe with multi-step phase-shift technique. *Optics and Lasers in Engineering*, 74:22–27, Nov 2015. ISSN 0143-8166.

Zhicheng Liu, Xilong Liu, Zhiqiang Cao, Xurong Gong, Min Tan, and Junzhi Yu. High precision calibration for three-dimensional vision-guided robot system. *IEEE Transactions on Industrial Electronics*, 70(1):624–634, 2023. ISSN 0278-0046.

William Lohry and Song Zhang. Genetic method to optimize binary dithering technique for high-quality fringe generation. *Optics Letters*, 38(4):540–542, 2013. ISSN 0146-9592.

Lei Lu, Jiangtao Xi, Yanguang Yu, and Qinghua Guo. Improving the accuracy performance of phase-shifting profilometry for the measurement of objects in motion. *Optics Letters*, 39(23): 6715–6718, 2014. ISSN 0146-9592.

J Lv, F Da, and D Zheng. Projector defocusing profilometry based on sierra lite dithering algorithm. *Acta Optica Sinica*, 34(3):0312004, 2014.

P. Palojarvi, K. Maatta, and J. Kostamovaara. Integrated time-of-flight laser radar. In *Proceedings of the IEEE Instrumentation and Measurement Technology Conference and IMEKO TC7 Conference*, pp. 1378–1381, 1996.

W Purgathofer, R. F. Tobler, and M Geiler. Forced random dithering: improved threshold matrices for ordered dithering. In *Proceedings of the IEEE International Conference on Image Processing*, pp. 1032–1035, 1994.

Shuo Shan, Peng Xu, Wen Zhang, Ze Li, Jintao Liu, and Jianhua Wang. Error-diffusion-kernel parameters for binary pattern in 1-bit fringe projection profilometry. *Applied Optics*, 62(33): 8882–8893, 2023. ISSN 1559-128X.

Y. Wang, Z. Liu, C. Jiang, and S. Zhang. Motion induced phase error reduction using a filbert transform. *Optics Express*, 26(26):34224–34235, Dec 24 2018a. ISSN 1094-4087.

Yajun Wang and Song Zhang. Optimal pulse width modulation for sinusoidal fringe generation with projector defocusing. *Optics Letters*, 35(24):4121–4123, 2010. ISSN 0146-9592.

Yajun Wang and Song Zhang. Three-dimensional shape measurement with binary dithered patterns. *Applied Optics*, 51(27):6631–6636, 2012. ISSN 1559-128X.

Yajun Wang, Chufan Jiang, and Song Zhang. Double-pattern triangular pulse width modulation technique for high-accuracy high-speed 3d shape measurement. *Optics Express*, 25(24):30177–30188, 2017. ISSN 1094-4087.

Yajun Wang, Saptarshi Basu, and Beiwen Li. Binarized dual phase-shifting method for high-quality 3d shape measurement. *Applied Optics*, 57(23):6632–6639, Aug 10 2018b. ISSN 1559-128X.

Yajun Wang, Vignesh Suresh, and Beiwen Li. Motion-induced error reduction for binary defocusing profilometry via additional temporal sampling. *Optics Express*, 27(17):23948–23958, Aug 19 2019. ISSN 1094-4087.

Zhenzhou Wang. Review of real-time three-dimensional shape measurement techniques. *Measurement*, 156:107624, 2020. ISSN 0263-2241.

Zhoujie Wu, Wenbo Guo, Yueyang Li, Yihang Liu, and Qican Zhang. High-speed and high-efficiency three-dimensional shape measurement based on gray-coded light. *Photonics Research*, 8(6):819–829, Jun 1 2020. ISSN 2327-9125.

Zhoujie Wu, Wenbo Guo, Qican Zhang, Haoran Wang, Xunren Li, and Zhengdong Chen. Time-overlapping structured-light projection: high performance on 3d shape measurement for complex dynamic scenes. *Optics Express*, 30(13):22467–22486, Jun 20 2022. ISSN 1094-4087.

Jing Xu and Song Zhang. Status, challenges, and future perspectives of fringe projection profilometry. *Optics and Lasers in Engineering*, 135:106193, 2020. ISSN 0143-8166.

Yuqi Yang, Jiangping Zhu, Jun Luo, Fan Yang, and Pei Zhou. 3d imaging method based on binary encoded fringes with complementary symmetric error diffusion paths. *Applied Optics*, 64(10): 2339–2350, Apr 1 2025. ISSN 1559-128X.

Di You, Zhisheng You, Xiao Zhang, and Jiangping Zhu. High-quality 3d shape measurement with binary half truncated sinusoidal fringe pattern. *Optics and Lasers in Engineering*, 155:107046, Aug 2022a. ISSN 0143-8166.

Di You, Zhisheng You, Pei Zhou, and Jiangping Zhu. Theoretical analysis and experimental investigation of the floyd-steinberg-based fringe binary method with offset compensation for accurate 3d measurement. *Optics Express*, 30(15):26807–26823, 2022b. ISSN 1094-4087.

Yi Yu and Feipeng Da. Defocused projection model for phase-shifting profilometry with a large depth range. *Optics Express*, 29(15):23597–23610, Jul 19 2021. ISSN 1094-4087.

Guofeng Zhang, Shuming Yang, Pengyu Hu, and Huiwen Deng. Advances and prospects of vision-based 3d shape measurement methods. *Machines*, 10(2):124, 2022.

Song Zhang. High-resolution 3d profilometry with binary phase-shifting methods. *Applied Optics*, 50(12):1753–1757, Apr 20 2011. ISSN 1559-128X.

Z. Y. Zhang. A flexible new technique for camera calibration. *IEEE Transactions on Pattern Analysis and Machine Intelligence*, 22(11):1330–1334, 2000. ISSN 0162-8828.

Kai Zhong, Zhongwei Li, Yusheng Shi, Congjun Wang, and Yuzhen Lei. Fast phase measurement profilometry for arbitrary shape objects without phase unwrapping. *Optics and Lasers in Engineering*, 51(11):1213–1222, Nov 2013. ISSN 0143-8166.

Pei Zhou, Jiangping Zhu, Hailong Jing, Zhijuan Duan, Shiyong An, and Yanqiong Guo. Design and experimental study of sinusoidal structured light mask with "s" shaped binary coding. *Laser & Optoelectronics Progress*, 57(15):151203, 2020a. ISSN 1006-4125.

Pei Zhou, Xiaoyi Feng, Jun Luo, and Jiangping Zhu. Temporal-spatial binary encoding method based on dynamic threshold optimization for 3d shape measurement. *Optics Express*, 31(14): 23274–23293, 2023. ISSN 1094-4087.

Peng Zhou, Ning Cai, Ting Wang, Xiang-Qun Cao, and Bin Lin. High-quality 3d shape measurement by kernel-optimized high sinusoidal similarity dither patterns. *Applied Optics*, 59(34): 10645–10650, 2020b. ISSN 1559-128X.

Feipeng Zhu, Wenwen Liu, Hongjian Shi, and Xiaoyuan He. Accurate 3d measurement system and calibration for speckle projection method. *Optics and Lasers in Engineering*, 48(11):1132–1139, NOV 2010. ISSN 0143-8166.

Jiangping Zhu, Pei Zhou, Xianyu Su, and Zhisheng You. Accurate and fast 3d surface measurement with temporal-spatial binary encoding structured illumination. *Optics Express*, 24(25):28549–28560, Dec 12 2016. ISSN 1094-4087.

Jiangping Zhu, Jun Luo, Junlin Du, and Pei Zhou. Spatial-temporal binarization method via jointly optimizing diffusion kernel and quantization threshold for 3-d surface imaging. *IEEE Transactions on Instrumentation and Measurement*, 73:5009813, 2024. ISSN 0018-9456.

Chao Zuo, Qian Chen, Shijie Feng, Fangxiaoyu Feng, Guohua Gu, and Xiubao Sui. Optimized pulse width modulation pattern strategy for three-dimensional profilometry with projector defocusing. *Applied Optics*, 51(19):4477–4490, 2012. ISSN 1559-128X.

Chao Zuo, Shijie Feng, Lei Huang, Tianyang Tao, Wei Yin, and Qian Chen. Phase shifting algorithms for fringe projection profilometry: A review. *Optics and Lasers in Engineering*, 109: 23–59, 2018. ISSN 0143-8166.

A Appendix

A.1 Three-step phase shifting

To further evaluate the performance of ESC under the challenging three-step phase-shifting condition, experiments are conducted on three objects, namely rabbit, astronaut, and sphere. Except for the number of phase-shifting patterns, all experimental settings remain identical to those in the previous experiments. The comparison is performed among methods applicable to three-step phase shifting. Accordingly, SHM is omitted, while the extended-kernel (EK) method (Shan et al., 2023) is included as an alternative approach.

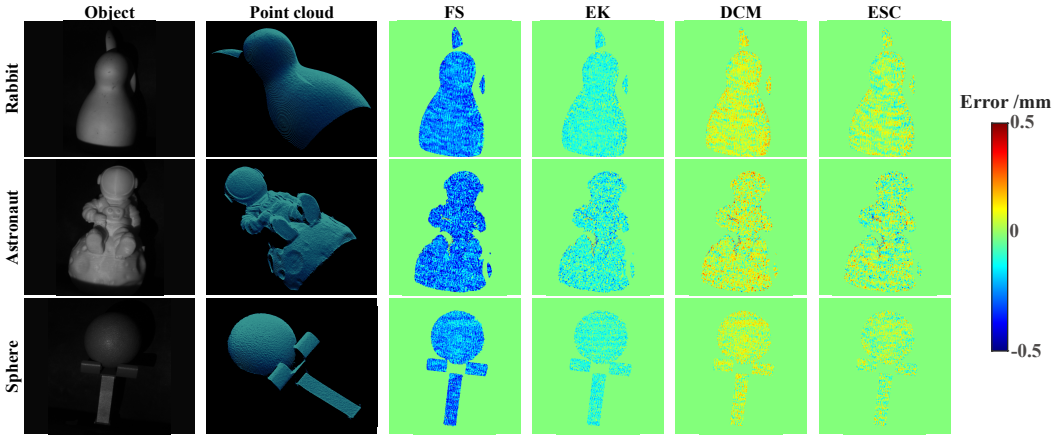

Figure 7: Point-cloud error distributions for different objects under three-step phase shifting. From top to bottom: the rabbit, astronaut, and sphere. From left to right: the measured objects, the reconstructed point clouds, and the error distributions obtained using FS, EK, DCM, and ESC.

Table 4: MAE/RMSE of point-cloud reconstruction for three-step phase shifting (unit: mm).

Object	FS	EK	DCM	ESC
Rabbit	0.245/0.448	0.086/0.175	**0.077/0.166**	**0.064/0.142**
Astronaut	0.260/0.436	0.101/0.193	**0.085/0.169**	**0.079/0.160**
Sphere	0.231/0.448	0.083/0.180	**0.073/0.164**	**0.064/0.148**

Fig. 7 shows the reconstructed point clouds and corresponding error distributions, and Table 4 summarizes the MAE and RMSE results. ESC achieves the lowest reconstruction errors among all compared methods for all three objects, demonstrating its effectiveness in suppressing binary quantization errors under three-step phase shifting. These results verify that ESC can maintain high reconstruction accuracy even when fewer phase-shifting patterns are used, providing a practical solution for high-speed 3D measurement scenarios.

A.2 Dynamic-scene measurement

To further evaluate the robustness of the proposed method under dynamic conditions, experiments were conducted using a high-speed FPP system. As illustrated in Fig. 8, the system consists of a DLP



Figure 8: FPP setup used for the dynamic experiments.

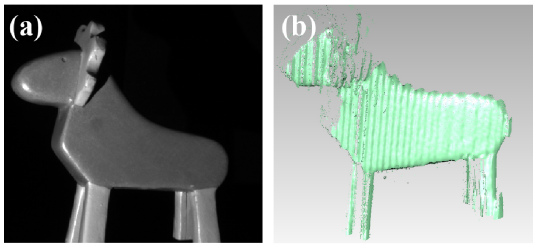

Figure 9: Measurement results in the 8-bit mode: (a) measured horse; (b) reconstructed horse.

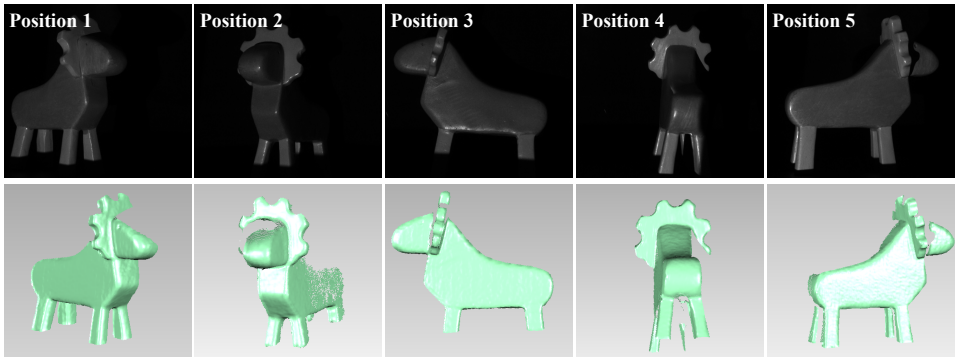

Figure 10: Dynamic 3D reconstruction of the horse by the ESC method.

projector (LightCrafter 4500), a high-speed camera (Basler acA640-750um, 640×480 pixels, up to 751 fps), and a rotating turntable operating at 3 RPM. A horse model was measured during rotation to simulate dynamic measurement scenarios. Phase decoding was performed using complementary Gray codes. For the 8-bit mode and ESC, five 15-pixel-period phase-shifted fringes combined with seven Gray-code patterns were used. The projector and camera operated at 20 fps for the 8-bit mode, while the binary modes achieved an acquisition rate of 556 fps.

Fig. 9 indicates that the 8-bit mode suffers from poor reconstruction quality, with obvious phase jumps caused by the misalignment between Gray codes and wrapped phase during motion, as well as ripple artifacts in the reconstructed regions. In contrast, Fig. 10 illustrates that ESC produces continuous and stable point clouds without obvious phase discontinuities, demonstrating that binary-fringe-based methods are more robust to motion.